Extended Uncertainty Analysis of a Multiprobe Antenna Measurement System for Complex Platform Testing

F. Saccardi[1], FELLOW AMTA, A. Giacomini[1], SENIOR AMTA, Jaydeep Singh[1], L. Foged[1], FELLOW AMTA, T. Blin[1], N. Gross[1], Arthur Romeijer[2]
(1) MVG, MICROWAVE VISION GROUP
(2) PULSAART BY AGC, Gosselies, Belgium

***Abstract*—This paper presents an extended uncertainty analysis of a multiprobe antenna measurement system developed for large platform testing across the 64 MHz to 6 GHz frequency range. Installed at the Pulsaart by AGC facility in Belgium, the system enables fast and accurate characterization of complex structures integrating multiple antennas. Building on previous studies, the analysis expands the uncertainty budget by including a broader set of antennas, such as monocones operating down to 50 MHz, and evaluating key figures of merit including radiation pattern, gain, efficiency, and cross-polarization. Particular emphasis is placed on reflectivity-related uncertainty, which is a dominant factor at lower frequencies due to chamber electrical size and absorber limitations. The methodology incorporates modal filtering and spatial displacement of antennas to isolate the environmental effects. The results offer detailed insights into antenna-dependent uncertainties and, for the first time, provide complete uncertainty estimations for the aforementioned metrics across the full operating frequency range.**

***Index Terms*— antenna, measurements, low frequency, multi-probe, spherical near field, uhf, uncertainty, vhf.**

I. INTRODUCTION

Technology advancements in communication technologies necessitate radiated testing encompassing the entire platform (e.g., automotive, defense, aerospace applications), which typically integrate numerous antennas [1]. Testing those antennas is critical to ensure proper performance after the integration on the platform. Consequently, antenna measurement systems with high accuracy and swift speeds have become essential. Spherical Near Field (SNF) testing techniques are favored for these applications due to their ability to precisely measure antennas with varying directivities and their minimal spatial footprint [1]-[6]. However, SNF technology requires comprehensive sampling, which results in extended testing times. Multi-Probe Array (MPA) systems effectively address this issue by capturing multiple sampling points simultaneously, thereby significantly reducing measurement times, often by factors of 5 to 10, depending on the frequency [5].

One such system is the spherical MPA system installed at the Pulsaart by AGC facility. This system is designed for thorough vehicle testing across the 64 MHz to 6 GHz frequency range. It features a hemispherical, 12-meter-diameter arch within a compact anechoic chamber, optimized with an absorber layout for the relevant frequency ranges. Its size allows for measuring large objects up to 6 meters and weighing up to 3 tons. This facility is ISO17025:2017 accredited by BELAC, which motivates this extended uncertainty budget study.

This paper presents new findings from an extensive measurement campaign to refine the system's uncertainty budget. The campaign focused on the error term associated with the residual reflectivity of the measurement environment, a significant contributor to overall measurement uncertainty at lower frequencies (e.g., VHF/UHF), where the relative size of anechoic chambers and absorbing materials is often insufficient compared to the wavelength [6]. The campaign included measurements of several reference antennas across different frequencies and positions to assess their interaction with the measurement environment (see examples in Figure 1).

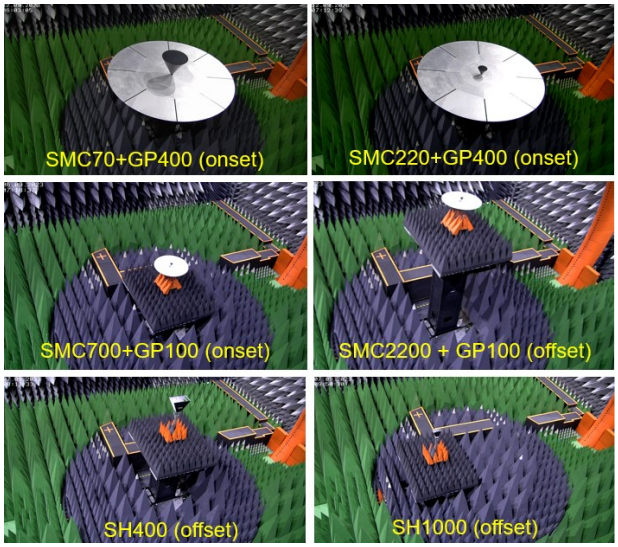

Figure 1. Photos of some antenna measuremement configurations in the MPA range at Pulsaart by AGC.

Preliminary uncertainty results were presented in [7], focusing on horn antennas and their radiation pattern figure of merit. This paper extends the analysis to monocone antennas covering the 50 MHz to 6 GHz frequency spectrum and considers additional antenna figures of merit such as gain, efficiency, and cross-polarization.

The paper provides valuable insights into the antenna-dependent uncertainty of MPA systems like the one under investigation, applicable to different frequency bands and various types of antennas. Although the main focus is on the investigation of the reflectivity, or room scattering term, the overall estimated uncertainties for the above-mentioned figure of merits are reported.

II. MPA System Uncertainty Evaluation

The MPA system at Pulsaart by AGC is a hemispherical, multi-probe antenna measurement facility designed for full-vehicle testing from 64 MHz to 6 GHz. The system features a lifting column to center vehicles within the coordinate system, minimizing sampling size. The scanning arch covers elevations from 0° (zenith) to 110° (20° below the horizon), enabling measurement of antenna radiation patterns below the horizon. The anechoic chamber uses pyramidal absorbers of various sizes (48" and 60") to support accurate measurements down to 64 MHz. The 6m radius MPA is split into two semiarches: one with 22 dual-polarized probes at 5° spacing for the 64–400 MHz band, and another with 111 dual-polarized probes at 1° spacing for the 0.4–6 GHz range. The ground floor, 2.5 m below the arch center and absorber-lined, includes a turntable for full 360° azimuth scanning. Periodic orthomodal calibration [8] is performed to equalize the probes' on-axis amplitude and phase response and to compensate for cross-polarization. Gain calibration is performed with the gain/efficiency substitution method [9]-[10] using two types of reference antennas, monocones and dual-ridged horns.

Building on the preliminary results presented in [7], in this extended study, the uncertainty evaluation has been broadened by including a larger set of antennas, monocone antennas (see Figure 1), which enable the analysis to be extended down to 50 MHz, which is even beyond the system's nominal lower frequency limit.

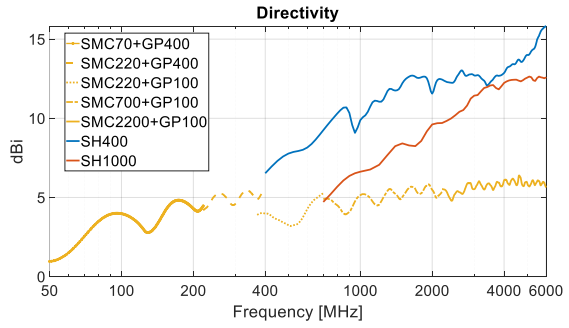

Figure 2. Nominal peak directivity over frequency of the horns (SHxxx) and monocones (SMCxxx) antennas considered in this investigation.

By incorporating antennas with varying directivity, ranging from omnidirectional monocones to more directive dual-ridge horns, the study captures a wide range of chamber illumination conditions across the 50 MHz to 6 GHz frequency range. The nominal peak directivity of all the considered antennas is reported in Figure 2. This diversity is essential for assessing how different antenna types interact with the measurement environment and excite potential residual reflections.

Table I: Measurement configurations.

Band [MHz]	SH400	SH1000	SMCxxx
50 – 220	-	-	Onset; Z=1.7m; X=1.0m
220 - 400			
400 - 700	Onset; Z=1.2m; Z=2.0m; X=1.5m		Onset; Z=2.0m; X=1.5m
700 - 2200		Onset; Z=2.0m; X=1.5m	
2200 - 4000	Onset; Z=1.2m; X=1.5m		
4000 - 6000	Onset; Z=1.2m; X=1.2m	Onset; Z=1.2m; X=1.2m	

As in the previous analysis [7], each antenna was measured at multiple positions within the chamber. This displacement is used to further vary the interaction with the chamber walls, thereby enhancing the impact of residual reflectivity on the measured radiation patterns.

Table I provides a summary of the considered antennas, including their respective positions and measured frequencies. This expanded dataset enables a more thorough assessment of the reflectivity-related uncertainty term, a significant contributor at lower frequencies. It is important to note that the maximum offset of each configuration determines the largest test zone analyzed, defining the applicability of this analysis.

III. Radiation Pattern Uncertainty

This section presents the findings on the measurement uncertainty of the radiation pattern. For each antenna configuration, a first set of patterns has been obtained using the standard NF/FF transformation based on spherical wave expansion (SWE) [4]. A second set has been generated by applying MvEcho, a modal filtering technique designed to mitigate the impact of reflections [11]. Following the approach in [7], both datasets were used to isolate and quantify the uncertainty contribution due to chamber reflectivity.

Figure 3 illustrates radiation patterns for two monocone antennas, the SMC70+GP400 at 220 MHz and the SMC700+GP100 at 1 GHz. Solid and dotted lines represent co-polar and cross-polar components, respectively, while different colors indicate varying antenna displacements.

In an ideal measurement environment, different antenna displacements should yield identical patterns after field transformation. However, when modal filtering is not applied (left side), the discrepancies among patterns are primarily caused by residual reflections, followed by uncompensated probe pattern effects, and truncation errors [7]. When MvEcho is applied (right side), reflection-induced errors are significantly reduced, leaving probe pattern and truncation effects as the dominant sources of variation. This is clearly observed in the attenuation of ripple artifacts in the filtered patterns.

Similar to Figure 3, Figure 4 compares the radiation patterns of the SH1000 horn antenna measured at different positions, both with and without the application of MvEcho. As also noted in [7], MvEcho effectively suppresses fast-varying ripples caused by residual environmental reflections. However, a more noticeable deformation of the pattern appears, particularly when a lateral offset along the x-axis is introduced. This effect is attributed to stronger tapering introduced by the probe at higher frequencies (above 4 GHz).

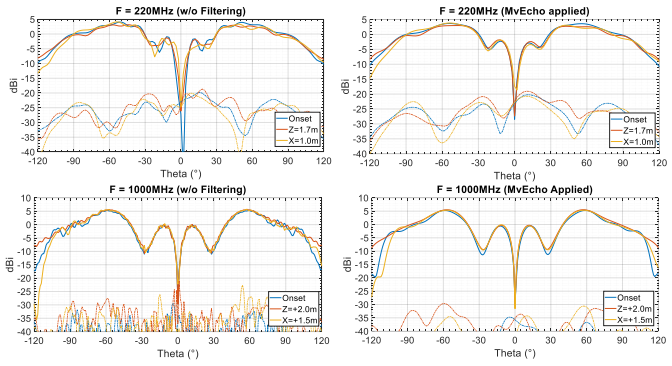

Figure 3. Measured radiation patterns of the SMC monocone antennas with (right) and without (left) MvEcho applied.

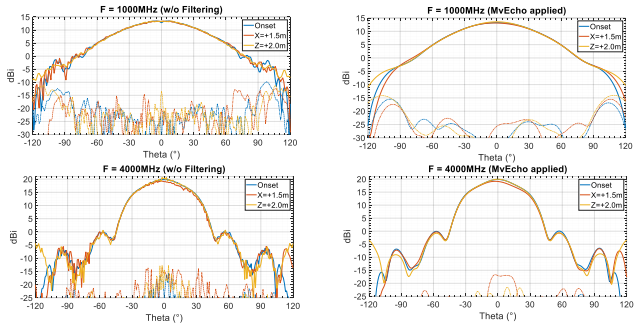

Figure 4. Measured radiation patterns of the SH1000 horn with (right) and without (left) MvEcho applied.

To concisely quantify the differences among measured radiation patterns, and thus the associated uncertainty, the global Equivalent Noise Level (ENL), defined in (1), is employed. This metric is derived by evaluating the ENL between each pair of radiation patterns, as shown in (2).

$$ENL_{global} = 20\log_{10}\left(\sqrt{\frac{\sum_{ij} 10^{ENL_{ij}/10}}{N}}\right) \quad (1)$$

$$ENL_{ij} = 20\log_{10}\left(RMS\left|\frac{E_i(\theta,\,\varphi) - E_j(\theta,\,\varphi)}{E_i(\theta,\,\varphi)_{MAX}}\right|\right) \quad (2)$$

Figure 5 presents the global ENL computed for each antenna across all measured frequencies. The ENL is calculated for both unfiltered patterns (dashed lines) and those processed with MvEcho (solid lines). As per the methodology adopted in this study, the uncertainty contribution due to reflectivity is inferred from the difference between the solid and dashed traces.

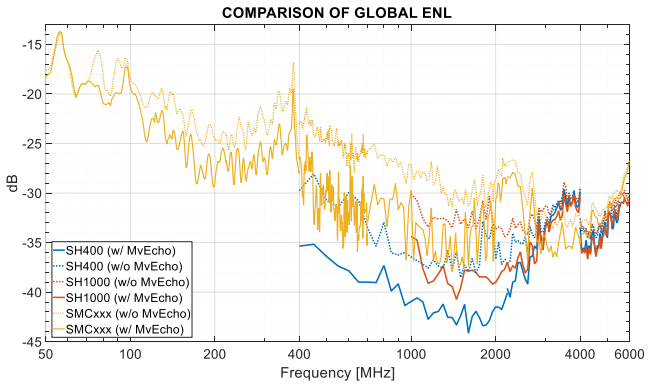

Figure 5. Global ENL for the measured antenna, with MvEcho (solid) and w/o processing (dotted).

A significant difference between the two processing methods is evident in many measurement scenarios. For instance, the monocone antennas (yellow traces) show a marked improvement in the 400 MHz–3 GHz range when MvEcho is applied, with the benefit diminishing at higher frequencies, consistent with the reduced impact of reflections at those frequencies. Similarly, the SH400 antenna (blue traces) shows improvement with MvEcho, though less pronounced due to its higher directivity and reduced chamber illumination.

At frequencies above 4 GHz, the global ENL increases, but the difference between filtered and unfiltered patterns narrows. These are respectively attributed to the more pronounced probe tapering effect (as also observed in Figure 4) and to the chamber's lower reflectivity at high frequencies.

Conversely, below 400 MHz, and especially below 220 MHz, the ENL rises again, while the effectiveness of MvEcho diminishes. In this range, reflections dominate the measurement uncertainty, and modal filtering is less effective. Therefore, below 220 MHz, the reflectivity contribution is directly estimated from the ENL of the unfiltered patterns.

Table II presents the reflection-related contribution to the radiation pattern uncertainty. The values in parentheses represent the global ENL, calculated as the Root Mean Square (RMS) over the specified frequency band. Taking as input the ENL traces shown in Figure 5, these global ENL are derived from the difference between global ENL obtained from the processing without modal filtering and those obtained using MvEcho. As previously mentioned, the only exception is the lowest frequency band (50–220 MHz), where MvEcho proves ineffective; in this case, the ENL is taken directly from the unfiltered processing.

The other values in Table II are the actual uncertainty contributions (ε) to the radiation pattern uncertainty. From the global ENL, these are computed using equation (3), assuming an Antenna Pattern Level (APL) of 0 dB, corresponding to the peak of the radiation pattern.

$$\varepsilon = 20log_{10}\left(1 + \frac{10^{ENL_{global}/20}}{10^{APL/20}}\right) \quad (3)$$

Table II: Reflections contribution to the radiation pattern uncertainty.

Band [MHz]	ε [dB, 1σ] (ENL_{global} [dB], 1σ)		
	SH400	SH1000	SMCxxx
50 – 220	-	-	±0.8 (-20.0)
220 - 400	-	-	±0.6 (-23.4)
400 - 700	±0.2 (-32.1)	-	±0.4 (-26.1)
700 - 2200	±0.1 (-37.6)	±0.2 (-33.9)	±0.2 (-30.8)
2200 - 4000	±0.1 (-39.8)	±0.1 (-36.6)	±0.2 (-35.1)
4000 - 6000	±0.1 (-39.6)	±0.1 (-38.0)	±0.1 (-38.9)

For brevity, the complete uncertainty budget of the radiation pattern measurement is not presented here. However, the final uncertainty estimation is summarized in Table III. This includes the updated reflection term derived from the current analysis (see Table II), along with all standard error contributions typical of a NF ranges [12], such as mechanical and RF-related errors. Although not detailed in this document, the analysis also enables a refined estimation of the probe probe pattern effect, which is uncompensated in this specific system.

Table III: Radiation Pattern Uncertainty at APL = 0 dB.

Band [MHz]	1σ-Uncertainty [dB]		
	SH400	SH1000	SMCxxx
50 – 220	-	-	±0.9
220 - 400	-	-	±0.7
400 - 700	±0.3	-	±0.5
700 - 2200	±0.3	±0.3	±0.4
2200 - 4000	±0.4	±0.4	±0.4
4000 - 6000	±0.4	±0.4	±0.4

IV. Upper Hemisphere Efficiency Uncertainty

In a quasi-hemispherical near-field (NF) system like the one under investigation, the efficiency cannot be directly measured due to power losses in the truncated area. While such losses are often negligible for highly directive antennas, the Upper Hemisphere Efficiency (UHE) is commonly used as a figure of merit [1]. As shown in (4), the UHE is calculated by integrating the gain-normalized radiation pattern over the forward hemisphere (i.e., θ = [0°, 90°]), rather than over the full sphere as in the case of total efficiency.

$$UHE = \int_{\varphi=0}^{360} \int_{\theta=0}^{90} G(\theta,\varphi) \sin\theta \, d\theta d\varphi \qquad (4)$$

This metric is particularly relevant in applications such as vehicle-mounted antennas, which are typically designed to radiate hemispherical patterns. Additionally, the UHE serves as a useful benchmark for comparing antenna losses across measurement ranges with varying degrees of truncation. Moreover, it is essential for accurate calibration of hemispherical NF systems using the efficiency-substitution method [9], which requires the measurement of a reference antenna with known UHE.

The calibration equation used to derive the UHE of an AUT is shown in (5), where $UHE_{raw,\,AUT}$ and $UHE_{raw,REF}$ are respectively the un-normalized UHE of the AUT and reference antenna measured in the MPA system and UHE_{REF} is the known UHE of the reference antenna. The uncertainty of UHE_{AUT} is obtained combining the uncertainties of each term in (5).

$$UHE_{AUT} = UHE_{raw,\,AUT} \frac{UHE_{REF}}{UHE_{raw,REF}} \qquad (5)$$

The uncertainties of both the $UHE_{raw,AUT}$ and $UHE_{raw,REF}$ terms have been estimated in the same manner. In particular, the measurement configurations detailed in Table I are considered and for each of them the UHE has been computed. For each antenna, Figure 6 illustrates the total UHE variation observed across different offsets (peak-to-peak, P2P). These variations are derived from non-filtered radiation patterns. Comparable results are obtained when MvEcho is applied, highlighting the robustness of the UHE metric against stray signals [9].

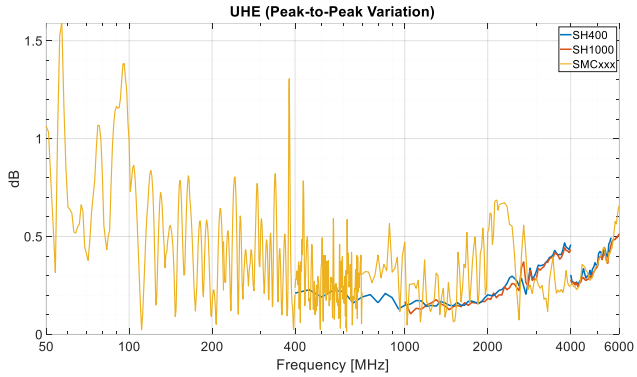

Figure 6. Comparison of UHE peak-to-peak variation (MvEcho not applied).

From the P2P variations shown in Figure 6, the standard deviation is calculated considering a scaling factor suitable to normalize such values to a Gaussian distribution [13]. Considering the effectiveness of the modal filtering via MvEcho above 400 MHz, the uncertainties of $UHE_{raw,AUT}$ and $UHE_{raw,REF}$ are estimated from the difference between the standard deviations of UHE with and without MvEcho. For the monocone antenna, this difference is found to be 0.1 dB in the 400–800 MHz band, and less than 0.1 dB for all antennas above 800 MHz. Conversely, at lower frequencies, due to the reduced effectiveness of MvEcho, the uncertainty due to reflections is directly estimated from the standard deviation of UHE without modal filtering. This results in uncertainties of 0.3 dB and 0.2 dB in the 50–220 MHz and 220–400 MHz bands, respectively.

Table IV: Raw UHE uncertainty.

Band [MHz]	1σ-Uncertainty [dB]		
	SH400	SH1000	SMCxxx
50 – 220	-	-	±0.4
220 - 400	-	-	±0.3
400 - 700	±0.2	-	±0.2
700 - 2200	±0.2	±0.2	±0.2
2200 - 4000	±0.2	±0.2	±0.2
4000 - 6000	±0.2	±0.2	±0.2

The estimated total raw-UHE uncertainty is reported in Table IV and is applicable to both the $UHE_{raw,AUT}$ and the $UHE_{raw,REF}$ terms. Although not detailed here, these uncertainty values are obtained taking into account the Root Sum Square (RSS) of the typical error terms of NF ranges [12]. Like the pattern uncertainty, these include RF error sources accounting for the above discussed reflectivity uncertainty, the residual probe pattern errors and mechanical errors.

The uncertainty associated with the reference efficiency values (UHE_{REF}) is now addressed. Although both SMC monocone and SH horn antennas are commonly used for gain calibration in this measurement system, this uncertainty analysis assumes the use of monocone antennas throughout the entire 50 MHz to 6 GHz band.

As previously noted [6], [10], the characterization of large antennas, such as the SMC70 and SMC220 mounted on a 4-meter ground plane, is carried out by leveraging the scalability properties of the SMC [10]. This approach is necessary due to the limited availability of accredited facilities capable of accommodating such large antennas. Instead, 10:1 scaled versions are measured in a standard reference facility at ten times the original frequency, preserving the antennas' electrical size.

While the dimensions and dielectric properties of the scaled antennas can be controlled during manufacturing, the conductivity, and therefore the Ohmic losses (OL), cannot be easily scaled [2]. As a result, the reference UHE is determined by separately evaluating the OL and Mismatch Loss (ML). The ML is obtained from the return loss measurements of the full-scale antenna, while the OL is estimated by measuring the radiation efficiency of the scaled antenna in the reference facility. Since the scaled antenna operates at higher frequencies, it is expected to exhibit greater losses than the full-scale version (assuming the same conductive material are used in both cases). Measurements indicate that the OL of the scaled antenna are below 0.4 dB, which is therefore taken as a conservative upper bound for the full-scale antenna. Incorporating also the uncertainty associated with the ML, the estimated 1σ-uncertainty for UHE_{REF} in the 50–400 MHz band is approximately 0.5 dB. Above 400 MHz the same 0.5 dB is considered assuming that typical reference data are involved instead of actual data coming from dedicated calibration. It is pointed out that at this stage, such reported values represent a conservative worst-case estimate. Further analysis is currently underway to refine these figures.

Table V: Final UHE uncertainty.

Band [MHz]	1σ-Uncertainty [dB]		
	SH400	SH1000	SMCxxx
50 – 220	-	-	±0.7
220 - 400	-	-	±0.7
400 - 700	±0.6	-	±0.6
700 - 2200	±0.6	±0.6	±0.6
2200 - 4000	±0.6	±0.6	±0.6
4000 - 6000	±0.6	±0.6	±0.6

The final estimated uncertainty of the UHE, presented in Table V, is obtained by combining the uncertainty of the reference antenna values with those reported in Table IV using the RSS [13]. It is important to note that the uncertainty values from Table IV are included twice to address both the uncertainty of measured raw UHE of the refence antenna and of the AUT. In this way, no similarity between the two antennas is assumed (conservative assumption). Nevertheless, it is usually recommended to calibrate the system using reference antennas whose radiation characteristics closely match those of the AUT [9], [10]. This approach helps mitigate common errors inherent to the measurement range. In such cases, the resulting UHE uncertainty could be reduced.

V. Realized Gain Uncertainty

Similar to the UHE, the realized gain of an AUT is derived using the efficiency substitution method, as formulated in equation (6). The only difference from equation (5) is the use of $G_{raw,\,AUT}$, which represents the unnormalized measured radiation pattern of the AUT.

$$G_{AUT} = G_{raw,\,AUT}\frac{UHE_{REF}}{UHE_{raw,REF}} \tag{6}$$

As with the UHE case, the uncertainty of the realized gain is obtained by applying the RSS to the individual uncertainty terms in equation (6). Specifically, the uncertainties associated with UHE_{REF} and $UHE_{raw,REF}$, previously presented, are included in this analysis. For $G_{raw,\,AUT}$, the radiation pattern uncertainty at an APL=0 dB, as reported in Table III, is considered.

The final 1σ-uncertainties of the realized gain are summarized in Table VI, across the different sub-bands and antenna types considered.

Table VI: Realized gain uncertainty.

Band [MHz]	1σ-Uncertainty [dB]		
	SH400	SH1000	SMCxxx
50 – 220	-	-	±1.1
220 - 400	-	-	±0.9
400 - 700	±0.6	-	±0.7
700 - 2200	±0.6	±0.6	±0.6
2200 - 4000	±0.7	±0.7	±0.7
4000 - 6000	±0.7	±0.7	±0.7

VI. Cross-Polar Uncertainty

This section addresses the cross-polarization (cx-polar) uncertainty, which is being presented for the first time for this type of measurement system and should therefore be considered preliminary.

In MPA systems, the cx-polar uncertainty is strongly influenced by the accuracy of the orthomodal calibration. This calibration not only equalizes the complex probe response but also enhances the cx-polar performance of the probes. As described in [8], the procedure relies on a linearly polarized calibration antenna, whose cx-polar is assumed to be ideal. However, any residual cx-polar component in the calibration antenna directly contributes to measurement uncertainty and must be accounted for in the budget.

For this analysis, it is assumed that the on-axis cx-polar level of the calibration antenna is -25 dB relative to the peak at the lowest frequency band (50–220 MHz), gradually improving to -40 dB at 700 MHz and remaining constant up to 6 GHz. These values represent worst-case estimates (approx. 3σ-confidence), and corresponding 1σ-values are used in the uncertainty budget, assuming a Gaussian distribution.

In the case of linearly polarized AUTs, azimuthal misalignment also affects cx-polar accuracy. A maximum misalignment of ±0.5° is estimated, corresponding to an introduced cx-polar level of -41 dB across the whole frequency range. Assuming an uniform distribution [14] and converting it to an equivalent Gaussian distribution, a value of -46 dB is used in the budget. This contribution is considered twice to account for potential misalignment of both the AUT and the calibration antenna, which are equally probable.

Finally, measurements from various antenna configurations have been used to estimate the cx-polar uncertainty contribution due to reflections. This is done using the same global ENL-based approach defined in (1), but applied to the cx-polar radiation patterns. The results are summarized in Table VII.

Table VII: Reflection contribution to cx-polar uncertainty.

Band [MHz]	Global ENL [dB, 1σ]		
	SH400	SH1000	SMCxxx
50 – 220	-	-	-27.2
220 - 400	-	-	-33.4
400 - 700	-37.9	-	-36.3
700 - 2200	-42.8	-39.6	-41.4
2200 - 4000	-44.8	-42.6	-41.1
4000 - 6000	-46.4	-45.1	-48.8

By combining all the aforementioned error sources using the RSS, the overall 1σ-uncertainty estimation for the cx-polar is presented in Table VIII. These values should be interpreted as the maximum measurable cx-polar level within the investigated measurement range, or, in other words, as the cx-polar induced by the measurement system itself.

Table VIII: Equivalent cx-polar introduced by the measurement system.

Band [MHz]	Cx-polar [dB, 1σ]		
	SH400	SH1000	SMCxxx
50 – 220	-	-	-26.3
220 - 400	-	-	-31.8
400 - 700	-35.5	-	-34.6
700 - 2200	-38.3	-36.9	-37.8
2200 - 4000	-39.0	-38.3	-37.6
4000 - 6000	-39.3	-39.1	-39.7

VII. Conclusions

A comprehensive uncertainty analysis of the multiprobe antenna measurement system installed at the Pulsaart by AGC facility has been presented in this paper. Although the system was originally designed for fast and accurate testing of large platforms within the 64 MHz to 6 GHz frequency range, the analysis has been successfully extended down to 50 MHz. Excellent performance has been demonstrated, particularly at low frequencies, where accurate antenna measurements are traditionally difficult due to limitations in chamber size and absorber effectiveness.

Low uncertainty levels have been achieved for key figures of merit, such as radiation pattern, gain, efficiency, and cross-polarization, while fast acquisition times are maintained through the use of the multiprobe array architecture. A diverse set of antennas, ranging from omnidirectional monocones to more directive horns, has been employed to provide varied illuminations of the test environment, enabling a robust characterization of the system's uncertainty. Environmental effects related to residual reflectivity have been effectively isolated through the application of modal filtering and spatial displacement techniques.

Future work will involve extending the uncertainty analysis to additional metrics such as phase accuracy and refining critical contributors, with particular attention given to the uncertainty associated with the reference antennas used in the gain calibration process. Moreover, additional work is currently on-going to enhance the orthomodal calibration antennas, with the objective of improving the system calibration in the lowest frequency range, with focus on the cross-polarization performance.

References

[1] Foged, L.J and M. Sierra-Castaner, Modern Automotive Antenna Measurements, Artech House, Boston, Massachusetts, 2022.

[2] IEEE Std 149-2021 "IEEE Standard Test Procedures for Antennas"

[3] IEEE Std 1720-2012 "Recommended Practice for Near-Field Antenna Measurements"

[4] J. E. Hansen (ed.), Spherical Near-Field Antenna Measurements, Peter Peregrinus Ltd., on behalf of IEE, London, United Kingdom, 1988

[5] P. Noren et al., "State of the art spherical near-field antenna test systems for full vehicle testing", 6th European Conference on Antennas and Propagation, EuCAP 2012, March 2012, Prague, Czech Republic;

[6] F. Saccardi, A. Giacomini, N. Gross, T. Blin, P.O. Iversen, L. J. Foged, "VHF/UHF Antenna Measurements Based on Multi Probe Array Technology" EuCAP 2024, Glasgow, Scotland.

[7] F. Saccardi et al. "Uncertainty Analysis of a Multiprobe Antenna Measurement System for Full Vehicle Testing" AMTA 2024, Cincinnati OH, USA

[8] F. Saccardi et al., "Fast Multi-Probe Planar Near Field Measurements With Full Probe Compensation" EuCAP 2021, 22-26 March 2021, Düsseldorf, Germany

[9] F. Saccardi et al., "Accurate Calibration of Truncated Spherical Near Field Systems with Different Ground Floors using the Substitution Technique" AMTA 2019, October 6-11, San Diego, USA

[10] A. Giacomini, L. J. Foged, F. Saccardi "Gain and Efficiency Calibration Antennas for Low Frequency Automotive Measurement Systems" 2025 19th European Conference on Antennas and Propagation (EuCAP), Stockholm, Sweden, 2025

[11] https://www.mvg-world.com/en/products/antenna-measurement/software/mv-echo

[12] A. C. Newell, "Error analysis techniques for planar near-field measurements," in IEEE Transactions on Antennas and Propagation, vol. 36, no. 6, pp. 754-768, June 1988, doi: 10.1109/8.1177.

[13] ISO/IEC Guide 98-3:2008(E), Uncertainty of Measurement—Part 3: Guide to the Expression of Uncertainty in Measurement (GUM: 1995), 2008.

[14] L. Foged *et al*., "Error calculation techniques and their application to the Antenna Measurement Facility Comparison within the European Antenna Centre of Excellence," EuCAP 2007, Edinburgh, 2007